Research Article | Vol. 34, No. 17 / 24 Aug 2026 / Optics Express 31567
Optics EXPRESS

Molecular iodine at 508 nm: hyperfine spectroscopy and operating regimes for optical frequency references

M. Weller,[1,*] K. Rostan,[1] A. Friedrich,[2] J. Wüst,[1,2] M. Oswald,[2] F. Kuschewski,[2] T. Schuldt,[2] and C. Braxmaier[1,2,3]

[1] Institute of Microelectronics, Ulm University, Ulm, Germany
[2] DLR Institute of Quantum Technology, Ulm, Germany
[3] Center for Integrated Quantum Science and Technology (IQST), Ulm University, Ulm, Germany
[*] markus.weller@uni-ulm.de

Abstract: We investigated molecular iodine transitions near 508 nm as candidates for compact optical frequency references based on modulation transfer spectroscopy. Focusing on the R(41) 51–0 transition at 508.028 nm, we resolved and frequency-calibrated all 21 hyperfine components and determined their linewidths (Γ), signal-to-noise ratios (SNR), and figures of merit (SNR/Γ). We identified three particularly favorable components for laser frequency stabilization, a_1, a_2, and a_3, which provide strong error signals suitable for robust locking. For these components, we systematically studied the dependence of linewidth, SNR, and SNR/Γ on iodine vapor pressure, pump and probe power densities, and modulation index. From the combined measurements we identified practical operating regimes that provide a robust compromise between signal contrast and narrow linewidth. From the measured linewidth and SNR, we estimate a short-term fractional frequency instability of 2.9×10^{-14} at 1 s. The resulting data set and working-point guidelines provide a quantitative basis for designing and optimizing iodine-stabilized frequency references at 508 nm and may serve as a useful starting point for neighboring transitions in this spectral region, supporting future metrology and space optical clock applications.

Published by Optica Publishing Group under the terms of the Creative Commons Attribution 4.0 License. Further distribution of this work must maintain attribution to the author(s) and the published article's title, journal citation, and DOI.

1. Introduction

Optical frequency references based on molecular iodine have become well-established tools in precision metrology, spaceborne instrumentation, and quantum technologies. Particularly in space applications, the combination of absolute frequency referencing, compactness, and robustness has made iodine-stabilized lasers promising candidates for next-generation Global Navigation Satellite System (GNSS) clocks [1] and fundamental physics missions, as demonstrated by the JOKARUS [2,3] sounding rocket mission and the upcoming COMPASSO [4,5] experiment aboard the International Space Station.

To date, most iodine frequency references have relied on Doppler-free spectroscopy of rovibronic transitions near 532 nm, where many hyperfine components exhibit favorable properties such as high contrast and narrow linewidths [6], and where highly stable laser systems are readily available and technology development for space instrumentation is ongoing [1,4]. These systems often utilize modulation transfer spectroscopy (MTS) [7] for robust frequency locking and have demonstrated fractional frequency instabilities in the low 10^{-15} range over averaging times of $\tau \approx 1$ s to 10^4 s under laboratory conditions [8]. Under flight conditions, the reported stability was in the low 10^{-11} range at $\tau \sim 1$ s, improving to the low 10^{-12} range by $\tau \sim 10^2$ s [3]. However, as precision requirements tighten and space-compatible integration becomes increasingly important,

#605121 https://doi.org/10.1364/OE.605121
Journal © 2026 Received 13 May 2026; revised 22 Jun 2026; accepted 26 Jun 2026; published 12 Aug 2026

Optics EXPRESS

interest has grown in exploring alternative iodine transitions that may offer narrower natural linewidths and thus improved frequency stability [9–12]. This trend is supported by rapid progress in narrow-linewidth external-cavity diode lasers, which have evolved from ~100 kHz-level designs in the 1990s to widely tunable kilohertz-level systems in recent years [13], making wavelengths beyond 532 nm increasingly accessible. Systematic spectroscopic studies by Cheng *et al.* [9] spanning the 498-523 nm region identified transitions near 508 nm that exhibited the narrowest observed natural linewidths, down to approximately 50 kHz (HWHM), making this wavelength range particularly promising.

In this work, we present a comprehensive spectroscopic study of hyperfine iodine transitions near 508 nm. Using the MTS technique, we resolved and characterized all 21 hyperfine components of the $R(41)$ 51–0 transition around 508.028 nm. For selected lines, we determined linewidths, signal-to-noise ratios, and figures of merit, and investigated their dependence on key experimental parameters, including pump power density, probe power density, vapor pressure, and modulation index. By fitting MTS-based theoretical models to the measured data, we obtain a consistent description of the line shapes and parameter dependencies for these transitions at 508 nm.

Our aim is to provide the first systematic data set and modeling framework for iodine transitions near 508 nm, thereby assessing their suitability for high-stability optical frequency references. Beyond immediate spectroscopic interest, the identified parameter dependencies allow us to propose optimal working points for future reference systems and to support the development of compact, robust iodine-stabilized lasers for metrology and space applications.

2. Experimental setup

The experimental setup is based on free-space optics in a breadboard-style arrangement using commercial off-the-shelf components, serving as a flexible testbed for high-resolution spectroscopy of iodine hyperfine transitions near 508 nm. A schematic overview is shown in Fig. 1.

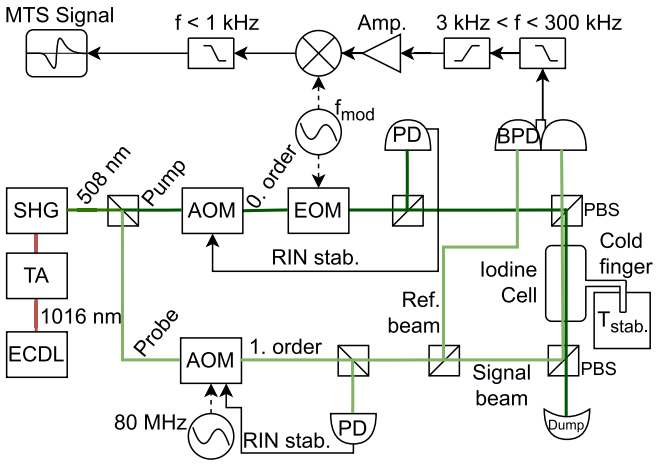


Fig. 1. Functional block diagram of the experimental setup. The 508 nm beam is split into pump and probe arms, both intensity-stabilized via AOMs with PD feedback. The probe beam uses the first diffraction order to introduce an 80 MHz offset, while the pump uses the zeroth order with active power stabilization. The pump is phase-modulated by an EOM at f_{mod}, and both beams are overlapped in a triple-pass iodine cell. The transmitted probe is detected with a balanced photodetector (BPD), and the filtered, amplified, and demodulated signal yields the MTS error signal.

Optics EXPRESS

The laser source consists of an external-cavity diode laser operating at 1016 nm, whose output is amplified by a tapered amplifier and subsequently frequency-doubled by means of a nonlinear second-harmonic-generation (SHG) crystal installed in a bow-tie enhancement cavity to generate light at 508 nm.

The light is divided into pump and probe beams, which are both intensity-stabilized by acousto-optic modulators (AOMs) in conjunction with photodiode (PD) feedback to suppress relative intensity noise (RIN). To mitigate parasitic interference effects, one AOM is used in first diffraction order, resulting in a frequency separation of 80 MHz between pump and probe, which is above the bandwidth limit of the photodetector. Utilizing an electro-optic modulator (EOM), the pump beam is subjected to phase modulation at the modulation frequency f_{mod} set to 96 kHz. The linear polarized beams are overlapped by means of polarizing beam splitters (PBS) and counter-propagating in a cross-polarized manner through a 30 cm iodine vapor cell in a triple-pass configuration, corresponding to an effective interaction length of 90 cm. This length was chosen as a practical compromise between signal strength and system compactness: modeling of iodine MTS at 532 nm predicts diminishing returns for longer cells, with lengths $\gtrsim 1$ m already close to the maximum signal level [14], and a recent stability analysis likewise reports only marginal improvement for interaction lengths beyond 2 m [15].

The transmitted probe is detected with a balanced photodetector (BPD), where a reference beam enables effective suppression of common-mode intensity noise. The detector output is subsequently bandpass-filtered and amplified, after which demodulation and low-pass filtering yield the MTS error signal. By sweeping the injection current of the ECDL, the laser frequency is scanned across the transitions, rendering the hyperfine resonances visible as dispersive features. These signals serve as the primary spectroscopic observables for the measurements presented in this work.

The iodine vapor pressure is controlled via a temperature-stabilized cold finger attached to the spectroscopy cell. Since the vapor pressure is uniquely determined by the solid-phase iodine temperature, precise stabilization of the cold finger allows reproducible control of the gas pressure over the full range relevant for pressure-broadening investigations.

3. Spectroscopy investigations

To evaluate the suitability of hyperfine iodine transitions near 508 nm for frequency stabilization, a detailed spectroscopic investigation was conducted of a Doppler-broadened absorption line centered at approximately 508.028 nm, which was selected because it exhibited the strongest absorption in its spectral vicinity among the transitions accessible with the current laser setup. This line corresponds to entry 1255 in the *Atlas du spectre d'absorption de la molécule d'iode* [16]. It lies in close spectral proximity to the R(20) 50–0 b_5 component at 508.077 nm, which was reported by Cheng *et al.* [9,10] to exhibit the narrowest natural linewidth in their survey of the 498-523 nm range. Although the tuning range of the laser system did not allow direct access to the R(20) line, the selected transition at 508.028 nm features strong absorption and narrow sub-Doppler features, making it an excellent candidate for initial studies. It should be noted, however, that any linewidths observed are strongly transition-dependent and not all hyperfine lines around 508 nm feature equally narrow linewidths. Even within a narrow wavelength interval, the natural linewidth and practical spectroscopic performance can vary with the rovibrational branch, rotational quantum number, and hyperfine component.

According to the iodine atlas, the Doppler-broadened feature labeled 1255 is associated with the rovibrational transition R(41) 51–0. Although the atlas additionally lists a second overlapping line, P(50) 64–1, this feature is either too weak to be detected or spectrally overlaps with components of the stronger transition. Only 21 hyperfine lines are resolved in the sub-Doppler spectrum, which strongly suggests that the observed signal originates exclusively from the R(41) transition. This is consistent with the hyperfine structure expected for odd rotational quantum

Optics EXPRESS

numbers, where the nuclear spin interaction of the iodine nucleus ($I = 5/2$) leads to 21 allowed hyperfine components arising from combinations of $F = J + I$ and associated selection rules. Such patterns are well documented for odd-J transitions in iodine and provide a characteristic fingerprint of the rotational state involved [10,17].

3.1. Full hyperfine spectrum and line characterization

To resolve the hyperfine structure of the transition, the laser frequency was swept across the full Doppler-broadened feature while recording the modulation transfer spectroscopy (MTS) signal, rendering the hyperfine resonances as dispersive features. For frequency calibration, we employed an independent auxiliary iodine reference at 508 nm (separate laser system and spectroscopy setup, MTS lock to the same $R(41)$ 51–0 manifold), which served solely as a frequency reference for heterodyne beat measurements. The two lasers were locked to the a_1 and a_{21} hyperfine components, respectively, and their beat note was recorded to calibrate the frequency axis with an absolute frequency uncertainty below 500 Hz (obtained from the measured beat instability and corrected for the 80 MHz offset introduced by the AOM). The measured MTS spectrum, shown in Fig. 2, reveals all 21 hyperfine components.

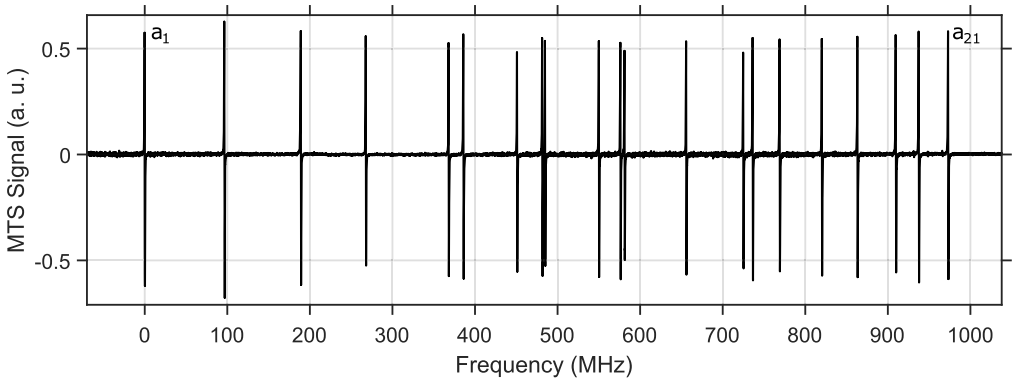


Fig. 2. MTS signal showing 21 hyperfine components of the R(41) 51–0 transition centered at 508.028 nm. The frequency axis is calibrated from the beat between the spectroscopy laser locked to a_{21} and an auxiliary reference laser locked to a_1. Relative positions and line shapes are obtained from fits to the MTS model (Eq. (1)) and listed in Table 1.

For the exact frequency interval values listed in Table 1, a sequential locking procedure was used: during the measurement series the auxiliary reference laser remained stabilized to a_1, while the main laser system was, in turn, locked to each individual hyperfine component a_k. For each k the heterodyne beat between both lasers was recorded and its frequency averaged to obtain the precise offset $\nu(a_k) - \nu(a_1)$. This approach suppresses scan-nonlinearity systematics and ties all tabulated intervals to the same common reference (a_1).

Linewidths (Γ), signal-to-noise ratios (SNR), and the figure of merit SNR/Γ were extracted by fitting the MTS resonances with the standard first-harmonic MTS response including adjacent sideband-mixing terms [7]:

$$S_{\mathrm{MTS}}(\omega) = \sum_{n=-N}^{N} J_n(\beta)\, J_{n-1}(\beta)\Big[\big(L_n(\omega) + L_{n-1}(\omega)\big)\cos\phi + \big(D_n(\omega) - D_{n-1}(\omega)\big)\sin\phi\Big],$$
$$\text{where } L_j(\omega) = \frac{1}{1+x_j^2}, \qquad D_j(\omega) = L_j(\omega)\, x_j, \qquad x_j(\omega) = \frac{\omega - \omega_0 - j\,\omega_m}{\Gamma}, \tag{1}$$

Optics EXPRESS

Table 1. Properties of the 21 hyperfine components of the R(41) 51–0 transition centered at 508.028 nm. Uncertainty of the frequency offsets is below ± 0.5 kHz. The three highest SNR/Γ values are marked: † first, ‡ second, ⋆ third.

Line	Frequency offset (MHz)	Γ HWHM (kHz)	SNR	SNR/Γ (1/MHz)
a_1	0.0000	364 ± 13	413 ± 9	1136 ± 70
$a_2^{\dagger}$	99.2757	349 ± 12	476 ± 10	1366 ± 49
a_3	193.4718	368 ± 9	442 ± 10	1203 ± 50
a_4	272.8234	348 ± 5	387 ± 8	1113 ± 28
a_5	372.2911	356 ± 17	415 ± 9	1165 ± 60
a_6	389.5628	405 ± 14	419 ± 8	1034 ± 41
a_7	452.0895	322 ± 8	378 ± 8	1175 ± 40
a_8	483.6732	344 ± 36	410 ± 15	1192 ± 131
a_9	487.1873	337 ± 23	407 ± 10	1207 ± 85
a_{10}	554.3268	345 ± 18	415 ± 9	1204 ± 68
$a_{11}^{\ddagger}$	581.0744	338 ± 11	420 ± 9	1243 ± 48
a_{12}	586.1555	323 ± 11	358 ± 8	1110 ± 44
a_{13}	662.2933	336 ± 8	395 ± 8	1177 ± 37
a_{14}	731.9820	330 ± 18	377 ± 8	1141 ± 68
a_{15}	743.4513	360 ± 8	408 ± 8	1135 ± 35
a_{16}	776.1415	382 ± 30	386 ± 10	1008 ± 84
$a_{17}^{\star}$	826.5789	330 ± 17	409 ± 9	1238 ± 68
a_{18}	868.9092	346 ± 19	422 ± 9	1220 ± 73
a_{19}	913.7695	405 ± 42	411 ± 9	1017 ± 108
a_{20}	940.2400	390 ± 27	423 ± 10	1085 ± 81
a_{21}	973.0917	372 ± 14	428 ± 9	1151 ± 48

with β the phase-modulation index, ω_m the modulation frequency, ω_0 the line center, and Γ the effective half width at half maximum (HWHM) of the Lorentzian response. Throughout this work, Γ denotes the effective linewidth under the respective experimental conditions, including any contributions from broadening effects, and should not be interpreted as the natural linewidth of the transition. The model includes all adjacent sideband mixing terms $J_n(\beta)J_{n-1}(\beta)$ up to order N, allowing for contributions from higher-order sidebands at large modulation indices. The functions $L_j(\omega)$ and $D_j(\omega)$ describe the in-phase and quadrature Lorentzian response of the iodine transition for each pump sideband j. An overall scaling factor was applied during fitting to match the measured signal amplitude.

A representative zoom into the a_2 component is shown in Fig. 3, together with a fit using the MTS model (Eq. (1)), illustrating that the observed dispersive line shape is well captured by the model used to extract Γ as well as the peak-to-peak amplitude A_{Sig}.

The linewidth uncertainty corresponds to the 1σ parameter uncertainty of the nonlinear MTS fit (covariance from the Jacobian of the fitted model); values were also cross-validated using Lorentzian fits to saturated absorption data of the same lines. SNR values were consistently extracted using a common noise reference background determined near the a_4 component, where the DC-coupled balanced detector was adjusted to minimize the local noise floor in the measurement shown in Fig. 2. Since the detector optimum depends on the local Doppler background level, which varies across the 21 hyperfine components, independent tests were performed and confirmed that an equivalent noise-floor level can be reached for any of the lines

Optics EXPRESS

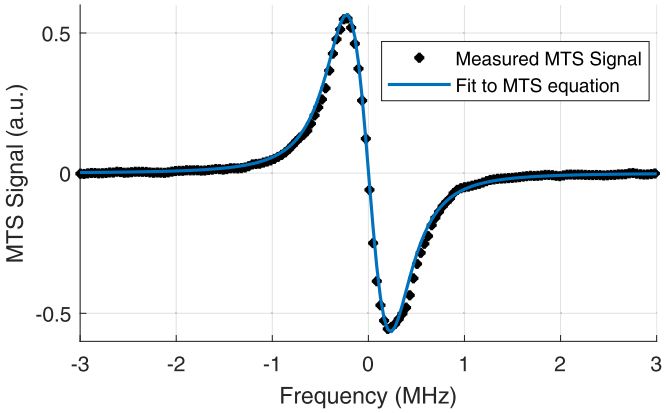


Fig. 3. Representative dispersive MTS feature (a_2 component of R(41) 51–0) with fit using the MTS model (Eq. (1)). From the fit the linewidth Γ and peak-to-peak signal amplitude A_{Sig} are extracted.

by re-optimizing the detector balance. Therefore, the noise-floor value determined near a_4 is used in the following analysis. Here, the SNR is defined as the fitted peak-to-peak MTS signal amplitude divided by the background-noise RMS,

$$\mathrm{SNR} = A_{Sig}/\sigma_N \quad \text{with} \quad \sigma_N = \sqrt{\hat{S}_0\,\mathrm{ENBW}}, \tag{2}$$

where $\hat{S}_0$ denotes the flat noise PSD level estimated from a Welch PSD of the background trace, and ENBW is the equivalent noise bandwidth of the 1 kHz demodulation low-pass filter [18]. The stated uncertainty values are the 1σ uncertainties, obtained by propagating in quadrature the 1σ uncertainties of the fitted amplitude and the noise, respectively. Point-wise uncertainties of the figure of merit, SNR/Γ, were obtained by standard quadrature uncertainty propagation from the SNR and Γ uncertainties.

The figure of merit, SNR/Γ, was used as a practical metric to evaluate the suitability of the line for frequency stabilization, since it directly enters the common estimation of the short-term fractional frequency instability $\sigma_y(\tau)$ [17]:

$$\sigma_y(\tau) \approx \frac{\Gamma}{\nu_0} \cdot \frac{1}{\mathrm{SNR}} \cdot \frac{1}{\sqrt{\tau}} \cdot G. \tag{3}$$

As a result, a large SNR/Γ value enables an improved short-term stability. The correction factor G accounts for the difference between the measurement bandwidth of the demodulated SNR and the effective bandwidth relevant for an Allan-deviation estimate; its definition is given in Appendix A.

A summary of the measured properties is provided in Table 1. Linewidths span 322–405 kHz and the SNR lies between 358 and 476, while SNR/Γ ranges from about 1008 to 1366 MHz^{-1}, with a_2 exhibiting the maximum. Components a_1, a_2, and a_3 were selected for detailed study both because of their high figures of merit and due to their favorable mutual spacing: the triplet is relatively isolated from neighboring features while being sufficiently separated from one another, which mitigates frequency hopping and supports robust long-term locking. The data were acquired under the following spectroscopy conditions: 1 Pa iodine vapor pressure, 8.6 mW pump power, 450 µW probe power, 2 mm beam diameter ($1/e^2$), and 90 cm interaction path length.

Optics EXPRESS

3.2. Dependence of linewidth and SNR on experimental parameters

To quantify how experimental conditions affect the spectroscopic signal, four series of measurements were performed in which the iodine vapor pressure, pump power, probe power, and modulation index were varied one at a time while all other parameters were kept fixed. For each series, we recorded both the linewidth Γ and the SNR of the a_1, a_2, and a_3 components, as shown in Figs. 4–7: the left panels display the linewidth as a function of the respective parameter, and the right panels show the corresponding SNR. In the following, beam powers are given as average power densities, $I = P/A_{\text{eff}}$, with $A_{\text{eff}} = \pi(d/2)^2$ and an effective beam diameter of $d = 2\,\text{mm}$, defined at the $1/e^2$ intensity level. Error bars indicate the 1σ uncertainties as defined in Section 3.1.

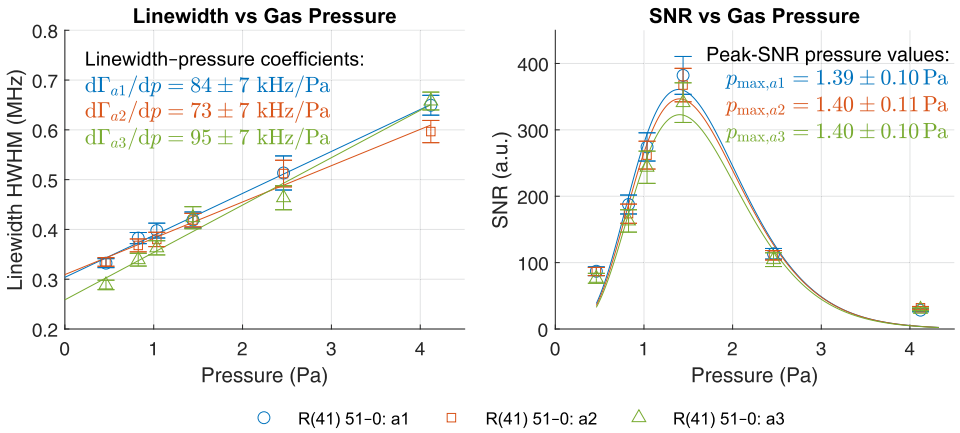


Fig. 4. Linewidth (left) and SNR (right) of the a1, a2, and a3 hyperfine components of the R(41) 51–0 transition as a function of iodine vapor pressure. Pump power density was fixed at 2.55 mW/mm^2 and probe power density at 73 $\mu\text{W}/\text{mm}^2$; all other parameters were kept constant.

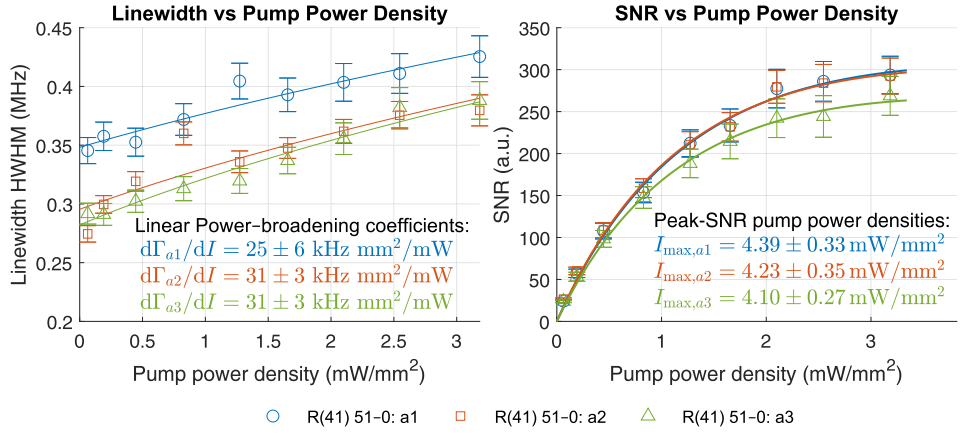


Fig. 5. Linewidth (left) and SNR (right) of the a1, a2, and a3 hyperfine components of the R(41) 51–0 transition as a function of pump power density. The iodine vapor pressure was fixed at 1.0 Pa; all other parameters were kept constant.

Optics EXPRESS

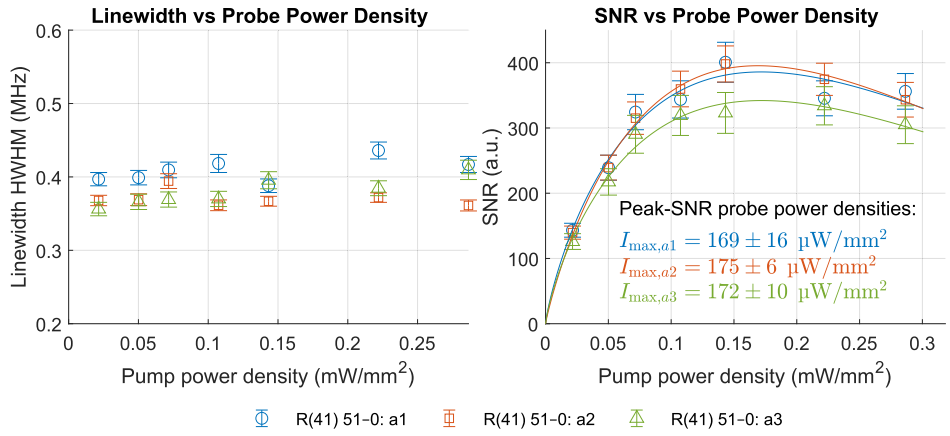


Fig. 6. Linewidth (left) and SNR (right) of the a1, a2, and a3 hyperfine components of the R(41) 51–0 transition as a function of probe power density. Pump power density was fixed at 2.55 mW/mm^2 and vapor pressure was fixed at 1.0 Pa; all other parameters were kept constant.

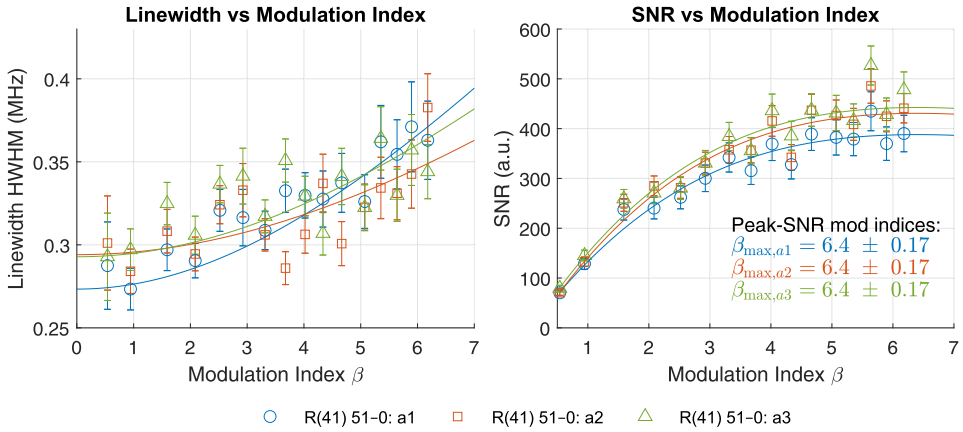


Fig. 7. Linewidth (left) and SNR (right) of the a1, a2, and a3 hyperfine components of the R(41) 51–0 transition as a function of modulation index β. The demodulation phase was fixed at $\phi = 0.93\pi$; all other parameters were kept constant.

3.2.1. Vapor-pressure dependence

As a first step, we investigated the influence of iodine vapor pressure on the line properties. The left panel of Fig. 4 shows the measured linewidths Γ of the a_1, a_2, and a_3 hyperfine components as a function of pressure between 0.46 Pa and 4.12 Pa. The pump power was kept constant at 2.55 mW/mm^2 pump power density to isolate collisional broadening, while the probe power density was set to 73 µW/mm^2. A second-order polynomial model [10] was initially tested but the quadratic terms were statistically insignificant and smaller than the fit residuals, indicating that the linewidth–pressure dependence is effectively linear in the investigated range. Consequently, a linear model

$$\Gamma(p) = \Gamma_0 + a\,p\,. \tag{4}$$

was adopted.

Optics EXPRESS

The pressure-broadening coefficients were obtained using a linear York regression [19], which accounts for uncertainties in both linewidth (from the individual MTS fits) and pressure. The pressure uncertainty was derived by propagating the thermistor uncertainty through the iodine temperature–vapor-pressure relation [20]:

$$\log_{10}(p) = -\frac{3512.83}{T} - 2.013\log_{10}(T) + 18.380, \tag{5}$$

with p in pascals and T in kelvin. The resulting coefficients are $d\Gamma_{a_1}/dp = 84 \pm 7$ kHz/Pa, $d\Gamma_{a_2}/dp = 73 \pm 7$ kHz/Pa, and $d\Gamma_{a_3}/dp = 95 \pm 7$ kHz/Pa. For comparison, literature reports values between 60–83 kHz/Pa for the R(56) 32–0:a10 line at 532 nm [17,21–24]. Extrapolation to zero pressure yields linewidths of 303 kHz, 309 kHz, and 256 kHz for a_1, a_2, and a_3, respectively (fit uncertainties below 5%).

The right panel of Fig. 4 shows the corresponding SNRs of the three hyperfine components. At very low pressures, the SNR is limited by the small molecular population in the vapor phase. With increasing pressure, the SNR rises, reaches a maximum, and then decreases again when excess absorption attenuates the pump/probe fields and degrades the demodulated signal. This qualitative behavior is consistent with simulations reported in the literature [17].

To determine the pressure at which the SNR is maximal, the data were fitted to an empirical model

$$\mathrm{SNR}(p) = A\,p^{n}\,e^{-Bp}, \tag{6}$$

with fit parameters A, n, and B, where the peak occurs at $p_{\max} = n/B$. Uncertainties on $p_{\max}$ were obtained by combining a statistical contribution from the nonlinear fit (delta method applied to the parameter covariance [25]) with a systematic pressure contribution obtained by refitting after coherent $\pm u_p$ perturbations of the pressure axis [26] (based on the thermistor uncertainty propagation as per Eq. (5)). The total 1σ uncertainty is the quadrature sum of these two components. From the fits we obtain $p_{\max,a1} = 1.39 \pm 0.10$ Pa, $p_{\max,a2} = 1.40 \pm 0.11$ Pa, and $p_{\max,a3} = 1.40 \pm 0.10$ Pa, as annotated in Fig. 4 (right).

3.2.2. Pump power dependence

Next, we examined the influence of pump power on the line properties. The left panel of Fig. 5 shows the measured linewidths of the a_1, a_2, and a_3 components as a function of pump power density in the range $0.032 - 3.185$ mW/mm^2 at a fixed iodine vapor pressure of $p = 1.0$ Pa. The observed linewidths were fitted using the power-broadening model [10,24]

$$\Gamma(I) = \frac{\Gamma_0}{2}\left(1 + \sqrt{1 + I/I_{\mathrm{sat}}}\right), \tag{7}$$

where I_{sat} denotes the saturation intensity specific to each transition. Over the investigated range, the dependence is approximately linear. The deviation between the nonlinear model and a linear fit remains below 20% of the 1σ York regression uncertainty for all three components, confirming that a linear approximation adequately describes the data. Linear power-broadening coefficients obtained from the York regression are $\mathrm{d}\Gamma_{a1}/\mathrm{d}I = 25 \pm 6$ kHz mm^2/mW, $\mathrm{d}\Gamma_{a2}/\mathrm{d}I = 31 \pm 3$ kHz mm^2/mW, and $\mathrm{d}\Gamma_{a3}/\mathrm{d}I = 31 \pm 3$ kHz mm^2/mW. From the fit, the saturation intensities were obtained as $I_{\mathrm{sat},a1} = 2.8$ mW/mm^2, $I_{\mathrm{sat},a2} = 1.9$ mW/mm^2, and $I_{\mathrm{sat},a3} = 1.6$ mW/mm^2. These saturation intensities are of the same order of magnitude as $I_{\mathrm{sat}} = 5.76$ mW mm^2 reported at 532 nm [24]. Given the higher vapour pressure of $p \simeq 3.9$ Pa in that work, our lower values at $p = 1.0$ Pa are reasonable. Moreover, extrapolation to zero pump power yields linewidths of approximately 348 kHz, 295 kHz, and 282 kHz for a_1, a_2, and a_3, respectively (fit uncertainties below 4%).

The right panel of Fig. 5 shows the corresponding SNR as a function of pump power density. Starting from the MTS response in Eq. (1) and assuming a resonant two-level medium, small

Optics EXPRESS

modulation index, and shot-noise-limited readout, the pump sets the saturation parameter ($s = I/I_{\mathrm{sat}}$). The pump provides a drive $\propto s$, while the demodulated MTS signal measures the derivative-like sensitivity of the bleached absorption, $\partial_s[1/(1+s)] = -1/(1+s)^2$. Their product yields an MTS amplitude $\propto s/(1+s)^2$. With white background noise dominating, the SNR follows the same scaling, which we fit with

$$\mathrm{SNR}(I) = 4\,\mathrm{SNR}_{\max}\,\frac{I/I_{Sat}}{\left(1+I/I_{Sat}\right)^2}, \tag{8}$$

peaking by construction at $I = I_{Sat}$. This captures the rapid low-power rise as the pump beam more effectively drives population modulation, enhancing the nonlinear four-wave mixing efficiency, and the high-power roll-off reflecting the diminishing sensitivity of the saturated transition while power broadening even reduces the probe's differential response to an already well saturated transition. From the fits we obtain $I_{\max,a1} = 4.39 \pm 0.33\,\mathrm{mW/mm^2}$, $I_{\max,a2} = 4.23 \pm 0.35\,\mathrm{mW/mm^2}$, and $I_{\max,a3} = 4.10 \pm 0.27\,\mathrm{mW/mm^2}$, as annotated in Fig. 5 (right).

3.2.3. Probe power dependence

Moreover, we investigated the influence of probe power while keeping the pump power and iodine pressure fixed. The left panel of Fig. 6 shows the measured linewidths of the a_1, a_2, and a_3 components as a function of probe power density. Assuming a low–probe–power regime, in which the probe contributes negligibly to the overall saturation, no power broadening is expected, consistent with the weak-absorption approximation described by Hopper [27]. The measurements confirm this expectation: within the experimental uncertainty, no systematic dependence of the linewidth on probe power density is observed over the investigated range.

The right panel of Fig. 6 displays the corresponding SNR as a function of probe power density. The signal rises rapidly at low probe power densities, reaches a broad maximum near $170\,\mu\mathrm{W/mm^2}$, and then decreases slightly. This behavior is expected in MTS: a stronger probe initially improves the detected modulation depth, but at higher levels the probe itself drives absorption and reduces the pump–probe transmission contrast, diminishing the demodulated signal. To describe this behavior, the data were fitted with the same empirical model as in Eq. (6), where the power-law term captures the strong initial increase at low probe power densities and the exponential term describes the gradual decline at higher probe power densities due to saturation; with a maximum occurring at $I = I_{\max}$. From the fits we obtain $I_{\max,a1} = 169 \pm 16\,\mu\mathrm{W/mm^2}$, $I_{\max,a2} = 175 \pm 6\,\mu\mathrm{W/mm^2}$, and $I_{\max,a3} = 172 \pm 10\,\mu\mathrm{W/mm^2}$, as annotated in Fig. 6 (right). In our settings this places the optimal probe power density well below $\sim 10\,\%$ of the pump power density, consistent with operating in a low–probe–power regime.

3.2.4. Modulation index dependence

Finally, we investigated the influence of the phase modulation index β applied to the pump beam via the resonant EOM. The left panel of Fig. 7 shows the measured linewidths of the a_1, a_2, and a_3 hyperfine components as a function of β. Over the investigated range, all three lines exhibit a slight but steady increase in linewidth with increasing β. This broadening arises because higher-order sidebands of the phase-modulated pump address displaced velocity classes in the iodine vapor, effectively averaging over multiple saturation features and widening the demodulated MTS signal (see Appendix B.3 for a detailed derivation).

To describe the observed broadening quantitatively, we model the linewidth as

$$\Gamma(\beta) \;=\; \frac{1}{2}\sqrt{W_0^2 \;+\; \alpha\,\beta^2 \;+\; C^2}\,, \tag{9}$$

where W_0 is the low-β width scale set by pressure broadening (Eq. (4)) and power broadening (Eq. (7)), α is an effective broadening coefficient that combines sideband-induced and technical

Optics EXPRESS

(RAM) contributions into a single β^2-dependent term, and C captures a constant width floor from transit-time broadening and residual first-order Doppler shifts. As shown in Appendix B.3, this three-parameter form arises from a more general four-parameter model in which the sideband spread function $R(\beta)$ is well approximated by $\beta^2/3$ over the experimental range, rendering the sideband and linear-broadening terms indistinguishable. The parameter set (W_0, α, C) is estimated for each hyperfine component via nonlinear least squares. This model reproduces the observed broadening for all three lines.

The right panel of Fig. 7 shows the corresponding behavior of the signal-to-noise ratio (SNR). At small modulation indices the SNR follows the increase of the effective first-order sideband amplitude, while at larger β the growth of higher-order sidebands slows down the further increase of the effective signal. To model this behavior, we used the envelope of the MTS signal amplitude as introduced in Eq. (1). Specifically, the signal envelope was calculated as [28]

$$M(\beta, \phi) = \max\left(S_{\beta,\phi}(\Delta)\right), \tag{10}$$

with $S_{\beta,\phi}(\Delta)$ given by Eq. (1). In accordance with our experimental procedure, the demodulation phase ϕ was kept fixed at the constant value $\phi = 0.93\pi$ for maximized signal amplitude as used in the measurements.

In our measurements, however, a linear increase in technical noise was observed for increasing β. To account for this effect, we extended the model by an empirical noise term $N(\beta) = 1 + \eta\,\beta$, so that the SNR is described as

$$\mathrm{SNR}(\beta) = \frac{A \cdot M(\beta, \phi_{\mathrm{fix}})}{N(\beta)} + S_0, \tag{11}$$

where A is an overall scale factor and S_0 accounts for a small β-independent SNR floor. The resulting fits are shown in Fig. 7 (right). We note that a direct comparison of the measured amplitude data with the model $M(\beta, \phi)$ also yielded excellent agreement (not shown here), confirming the consistency of the description. For all three investigated hyperfine components, the SNR reaches its maximum at $\beta = 6.4 \pm 0.17$.

3.3. Figure of merit SNR per linewidth

Finally, Fig. 8 shows the calculated figure of merit, defined as SNR/Γ, for the a_1, a_2, and a_3 components as a function of vapor pressure, pump power density, probe power density, and modulation index β. These values are derived from the previously measured linewidth and SNR data discussed above and represent the key metric for evaluating the short-term stability of a given transition, as discussed in Section 3.1. All four parameter scans qualitatively follow the shape of the corresponding SNR curves; however, the additional linewidth dependence makes the figure of merit more directly indicative of optimal operating conditions. For the modulation index, the $\mathrm{SNR}/\Gamma(\beta)$ data were fitted using the combined MTS envelope, noise, and linewidth model of Eq. (11), yielding broad, gently peaked maxima for all three lines and comparatively large uncertainties owing to the flatness of these peaks and the limited constraints on the linewidth fits. From these data, the following parameter values were identified as the most suitable operating points:

- Vapor pressure: 1.31 Pa (a_1), 1.31 Pa (a_2), 1.28 Pa (a_3),
- Pump power density: 3.19 mW/mm^2 (a_1), 3.03 mW/mm^2 (a_2), 2.46 mW/mm^2 (a_3),
- Probe power density: 162 µW/mm^2 (a_1), 175 µW/mm^2 (a_2), 156 µW/mm^2 (a_3),
- Modulation index: 4.8 (a_1), 5.6 (a_2), 6.3 (a_3).

Optics EXPRESS

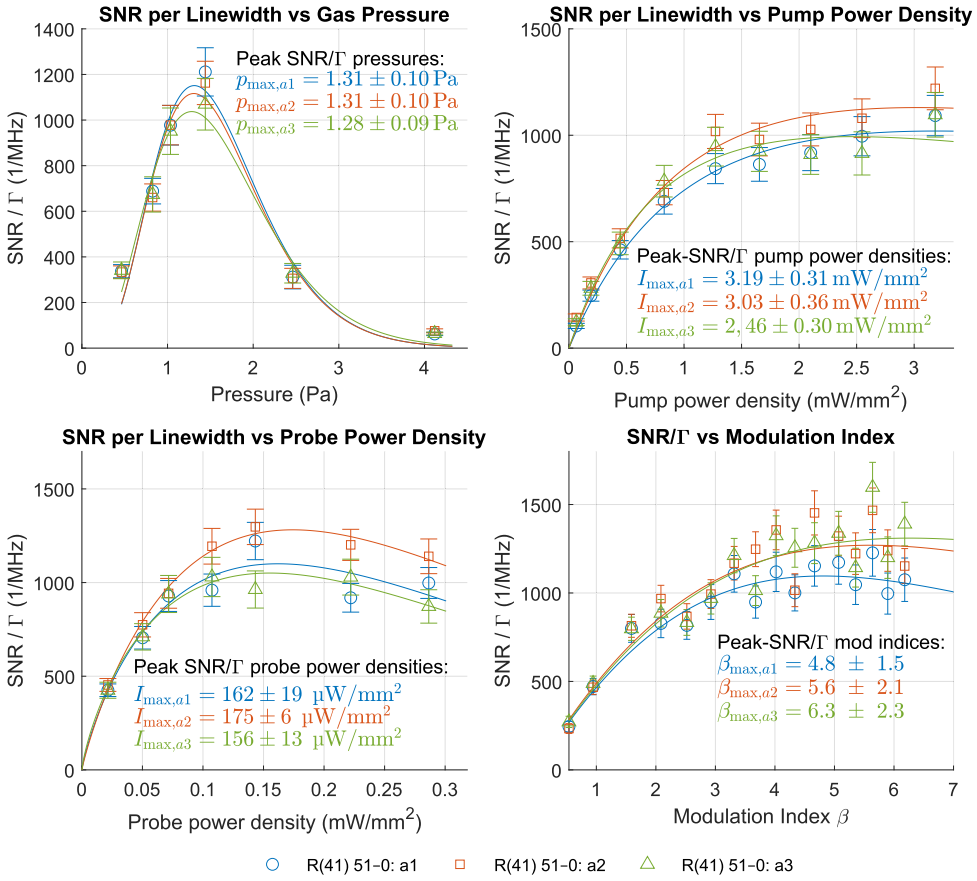


Fig. 8. Figure of merit SNR/Γ for the a_1, a_2, and a_3 components as a function of (top left) iodine vapor pressure, (top right) pump power density, (bottom left) probe power density, and (bottom right) modulation index β. Each plot reveals optimal parameters for frequency stabilization in terms of short-term stability according to Eq. (3).

These conditions represent the best compromise between signal strength and spectral sharpness and can be used as the basis for subsequent locking and stability considerations. While high pump power generally improves the figure of merit, the saturation-like behavior means that power densities exceeding approximately 1.5 mW/mm^2 already yield near-optimal performance. The broad maxima of SNR/Γ versus modulation index indicate a practical operating range of $4 \lesssim \beta \lesssim 8$, where the figure of merit remains close to its maximum and is relatively insensitive to small changes in β. This is in close agreement with the theoretically predicted optimum regime $3 \lesssim \beta \lesssim 10$ reported by Preuschoff *et al.* [29]. Overall, the parameter values identified here are not only relevant for the investigated a_1, a_2, and a_3 components, but also provide a valuable starting point for other hyperfine transitions in the 508 nm spectral region.

4. Discussion

In the broader context of iodine-based optical frequency references, transitions near 532 nm remain the established platform, supported by extensive atlas work [6], detailed characterization of line properties [24], and compact high-performance reference systems developed for metrological [8] and space-oriented applications [1]. At the same time, recent work at neighboring wavelengths

Optics EXPRESS

such as 514 nm [30–32] and 520.2 nm [12] has shown that the green spectral region beyond 532 nm remains technologically attractive, both for practical stabilized laser systems and for precision spectroscopy of previously less explored transitions .

Against this background, the specific role of the 508 nm region has so far remained unresolved. Earlier survey measurements by Cheng *et al.* identified transitions near 508 nm as particularly promising [9,33]. However, that work did not provide the transition-specific and parameter-dependent characterization required to assess practical suitability for laser frequency stabilization. The measurements presented fill this gap by providing, to our knowledge, the first systematic operation-oriented investigation of a molecular iodine transition at 508 nm.

The significance of these results is therefore not limited to the characterization of a single transition. Rather, they provide a quantitative bridge between earlier broad spectroscopic surveys and the practical design of future frequency references. In particular, the data presented identify which components are most favorable for locking, which parameter ranges provide the best compromise between narrow linewidth and strong error signal, and how these trade-offs compare with the expectations that motivated interest in the 508 nm region in the first place. In this sense, the work establishes 508 nm as a realistic candidate for compact iodine-stabilized optical references and provides a framework that can be transferred to neighboring rovibronic transitions in the same spectral region.

5. Conclusion and outlook

We have presented a systematic spectroscopic investigation of molecular iodine hyperfine transitions near 508 nm with a focus on their use as optical frequency references. Using modulation transfer spectroscopy, all 21 hyperfine components of the R(41) 51–0 transition at 508.028 nm were resolved and frequency-calibrated, and their linewidths, signal-to-noise ratios, and figures of merit were determined. This data set provides, to our knowledge, the first complete characterization of a 508 nm iodine transition at the level of detail required for laser frequency stabilization.

For the three most favorable components, a_1, a_2, and a_3, we mapped the dependence of linewidth, SNR, and SNR/Γ on iodine vapor pressure, pump and probe power densities, and modulation index. From these measurements, we identified practical operating regimes that offer a robust compromise between signal contrast and spectral sharpness. The resulting working points and parameter ranges constitute ready-to-use guidelines for designing and optimizing frequency references on this transition and may serve as a useful starting point for nearby iodine lines in the 508 nm region.

Using Eq. (3), a short-term instability projection is obtained by inserting the experimentally observed best-case values of Γ and SNR, together with ν_0 and the corresponding bandwidth correction. For the most favorable component, a_2, this yields an estimated fractional frequency instability of $\sigma_y(1\,\mathrm{s}) \approx 2.9 \times 10^{-14}$. Although the effective linewidth observed here is about a factor of 2–3 smaller than effective linewidths reported for typical 532 nm iodine systems ($\sim 800 - 900$ kHz HWHM [17,24]), the resulting instability estimate remains comparable to many 532 nm Refs. [4,6,34] and does not yet reach the best reported values [8]. This indicates that, in the present setup, the projected stability is not governed by linewidth alone but also by the achieved SNR, which depends on further implementation-specific factors such as interaction length and electronic readout noise.

The measurements and models reported here establish a quantitative basis for assessing the suitability of 508 nm iodine transitions as high-stability optical references and for projecting their short-term performance using standard instability estimates. Future work will extend this approach to additional rovibronic branches around 508 nm, include absolute frequency measurements, and transfer the identified operating regimes to more compact and environmentally robust reference systems aimed at metrology and spaceborne applications.

Optics EXPRESS

A. Definition of correction factor G

The SNR in this work is defined using the RMS noise at the output of the 1 kHz demodulation low-pass filter (Eq. (2)) and therefore corresponds to a measurement bandwidth set by the hardware. However, for a short-term instability estimate, continuous time-averaging acts as a narrower noise filter. For an Allan-deviation estimate, time averaging is equivalent to a noise filter with [35]

$$\mathrm{ENBW}_{\mathrm{Allan}}(\tau) = 0.476/\tau.$$

The effective bandwidth is thus

$$\mathrm{ENBW}_{\mathrm{eff}}(\tau) = \min(\mathrm{ENBW},\, 0.476/\tau)\,,$$

which can be expressed in Eq. (3) by the correction factor

$$G = \sqrt{\mathrm{ENBW}_{\mathrm{eff}}(\tau)\cdot\tau/\mathrm{ENBW}}.$$

In the present regime ($\tau \gg 0.476/\mathrm{ENBW}$) [36], this reduces to the constant

$$G = \sqrt{0.476/\mathrm{ENBW}},$$

avoiding double-counting of the demodulation bandwidth while preserving the $\propto 1/\sqrt{\tau}$ dependence for white frequency noise.

B. Theoretical models for MTS signal dependences

The empirical and semi-empirical models fitted to the experimental data in Sections 3 and 4 are motivated by the underlying physics of modulation transfer spectroscopy in an absorbing molecular vapor. This appendix provides compact derivations of these models, starting from the four-wave mixing (FWM) picture of MTS signal generation, the saturation response of a two-level medium, and the Jacobi–Anger decomposition of the phase-modulated pump field.

B.1. SNR versus pressure

The MTS signal originates from coherent four-wave mixing between the counter-propagating pump and probe beams mediated by the nonlinear susceptibility of the iodine vapor. At position z along a cell of length L, the local FWM contribution is proportional to the molecular number density $\mathcal{N} \propto p$ and to the local intensities of both beams. Because each beam undergoes linear absorption with coefficient $\alpha \propto p$, the pump intensity decays as $I_{\mathrm{pump}}(z) \propto e^{-\alpha z}$ while the counter-propagating probe decays as $I_{\mathrm{probe}}(z) \propto e^{-\alpha(L-z)}$. When the local FWM contributions are integrated over the cell length, the position-dependent attenuation factors combine to give a single exponential $e^{-\alpha z}\cdot e^{-\alpha(L-z)} = e^{-\alpha L}$, yielding a total signal proportional to

$$S_{\mathrm{tot}} \propto \mathcal{N}\, e^{-\alpha L} \propto p\, e^{-Bp},$$

where $B = \sigma_{\mathrm{abs}} L/(k_B T)$ collects the absorption cross-section and cell geometry into a single parameter with units of inverse pressure. This functional form predicts a linear rise of the signal at low pressures, where molecular density dominates, and an exponential roll-off at high pressures, where absorption of both beams suppresses the FWM process; the signal peaks at $p_{\max} = 1/B$.

In practice, several effects modify the low-pressure scaling from strictly p^1 to a more general power law p^n with n typically below unity. The dominant correction arises from pressure-dependent linewidth broadening: as described by Eq. (4), the homogeneous linewidth increases linearly with pressure, $\Gamma(p) = \Gamma_0 + ap$, and because the peak-to-peak MTS amplitude scales approximately as $1/\Gamma(p)^2$, the signal acquires a suppression factor $(\Gamma_0 + ap)^{-2}$ that reduces the

Optics EXPRESS

effective exponent. Additional corrections from position-dependent saturation along the cell and from the multi-pass beam geometry contribute further deviations. Treating the exponent n as a free parameter accommodates these effects and leads to Eq. (6),

$$\mathrm{SNR}(p) = A\, p^n\, e^{-Bp},$$

which peaks at $p_{\max} = n/B$.

B.2. SNR versus pump power density

The MTS signal is a third-order nonlinear optical process in which two pump photons create a population grating from which the probe beam scatters coherently into the detection channel. For a two-level system with on-resonance saturation parameter $s = I/I_{\mathrm{sat}}$, the population grating amplitude requires pump intensity and thus scales as s, while the effective nonlinear susceptibility of the saturation-broadened medium contributes a factor $1/(1+s)^2$ from the derivative of the saturated population difference with respect to the pump field. The heterodyne-detected MTS signal amplitude is therefore proportional to the product $s/(1+s)^2$. This function has a single maximum at $s = 1$, corresponding to $I = I_{\mathrm{sat}}$, with a peak value of $1/4$. The physical interpretation is that at low pump power densities the grating is weak, while at high pump power densities the transition is fully saturated and the medium's differential response vanishes, producing a broad optimum near the saturation threshold. Normalizing so that the maximum value equals $\mathrm{SNR}_{\max}$ yields Eq. (8),

$$\mathrm{SNR}(I) = 4\,\mathrm{SNR}_{\max}\,\frac{I/I_{\mathrm{sat}}}{\left(1 + I/I_{\mathrm{sat}}\right)^2},$$

where the prefactor of 4 compensates the $1/4$ peak value of $s/(1+s)^2$, ensuring $\mathrm{SNR}(I_{\mathrm{sat}}) = \mathrm{SNR}_{\max}$ by construction.

B.3. Linewidth versus modulation index

The Jacobi–Anger expansion decomposes the phase-modulated pump field into a comb of optical sidebands at frequencies $\omega_L + n\omega_m$ with amplitudes proportional to the Bessel functions $J_n(\beta)$. Each sideband carries intensity $I_n = I_0 J_n^2(\beta)$ and independently saturates the velocity class of iodine molecules centered at $v_n = n\omega_m/k_L$, burning a spectral hole of power-broadened half-width $\Gamma_2\sqrt{1 + s_0 J_n^2(\beta)}$, where $s_0 = I_0/I_{\mathrm{sat}}$ is the unsaturated pump parameter and Γ_2 is the homogeneous linewidth.

The first-harmonic MTS lineshape (Eq. (1)) receives contributions from adjacent sideband pairs $(n, n{+}1)$, each weighted by $w_n = [J_n(\beta)\, J_{n+1}(\beta)]^2$. Since the pair centered at index n probes velocity classes near $v \approx n\omega_m/k_L$, the effective spectral spread of the contributing pairs is characterized by the normalized second moment

$$R(\beta) = \frac{\sum_n n^2\, w_n}{\sum_n w_n}\,. \tag{12}$$

At small β only the two lowest-order pairs dominate and $R \to 1/2$. In the opposite limit $\beta \gg 1$, the Bessel functions $J_n(\beta)$ are approximately uniformly distributed with amplitude $\sim 1/\sqrt{\pi\beta}$ over the range $|n| \lesssim \beta$, so the weights w_n become nearly constant over $\sim 2\beta$ sideband orders. The normalized second moment of such a quasi-uniform distribution is $\langle n^2\rangle/1 \approx \beta^2/3$, the variance of a uniform distribution on $[-\beta, \beta]$, yielding

$$R(\beta) \;\approx\; \frac{\beta^2}{3}, \qquad (\beta \gtrsim 2). \tag{13}$$

Numerically, this approximation accounts for more than 99% of the variance of $R(\beta)$ over the experimental range $\beta \in [0, 7]$.

Optics EXPRESS

The observed MTS linewidth receives three independent contributions that add in quadrature, a standard approximation for broadening mechanisms of mixed Lorentzian and Gaussian character. The first is the saturation-broadened width modulated by sideband spread: the on-axis width $W_0 = 2\,\Gamma_2(p)\sqrt{1+s}$ from Eq. (7) is enhanced by the variance of the displaced sub-features to $W_0\sqrt{1 + A\,R(\beta)}$, where the dimensionless coefficient A implicitly contains the ratio ω_m/W_0. The second is a linear technical broadening term $B\beta$, arising primarily from residual amplitude modulation (RAM) of the electro-optic modulator crystal, whose parasitic intensity modulation grows in proportion to the applied modulation depth. The third is a constant floor C, independent of β, that captures transit-time broadening from the finite beam diameter and residual first-order Doppler shifts from imperfect beam overlap. Combining these three contributions in quadrature yields

$$\Gamma(\beta) = \tfrac{1}{2}\sqrt{[W_0\sqrt{1 + A\,R(\beta)}]^2 + (B\beta)^2 + C^2},$$

where the factor of $1/2$ converts from the FWHM-scale quantities W_0, $B\beta$, and C to the HWHM convention used throughout this paper.

Substituting Eq. (13) into the quadrature expression above collapses the sideband-broadening and linear-broadening terms into a single β^2-dependent contribution. Defining the effective broadening coefficient $\alpha \equiv W_0^2 A/3 + B^2$, the linewidth reduces to

$$\Gamma(\beta) \;\approx\; \tfrac{1}{2}\sqrt{W_0^2 + \alpha\,\beta^2 + C^2}, \tag{14}$$

which is the form effectively constrained by the data. Because the approximation Eq. (13) accounts for more than 99% of the variance of $R(\beta)$ over the experimental range, the sideband-broadening term $W_0^2 A\,R(\beta)$ and the linear-broadening term $(B\beta)^2$ are nearly perfectly degenerate under the square root, and only their sum α is identifiable from the fit. This degeneracy is reflected in the large individual parameter uncertainties reported in the main text. The model nevertheless provides an excellent description of the observed linewidth evolution; it should simply be interpreted as constraining the total β^2-dependent broadening rather than separately quantifying its sideband and technical contributions.

B.4. Signal envelope

The peak-to-peak amplitude of the MTS dispersive signal at a given modulation index β and demodulation phase ϕ is obtained by numerical maximization of the MTS lineshape (Eq. (1)) over the probe detuning Δ, as defined in Eq. (10). In the small-β regime, the Bessel expansion is dominated by the first-order sideband pair (J_0, J_1), whose product grows as $\beta/2$, so that $M \propto \beta$ and the signal rises linearly with modulation depth. As β increases beyond approximately 1.8 (where $|J_1|$ reaches its maximum), the pump power is redistributed among an increasing number of higher-order sidebands, each individually weaker. The signal envelope therefore saturates and eventually decreases at very large β, as no single sideband pair dominates the four-wave mixing process. Because the lineshape involves a sum over all contributing sideband pairs with β-dependent Bessel weights and frequency offsets, no closed-form expression for $M(\beta, \phi)$ is available for general β; the envelope is therefore computed numerically at each data point.

B.5. SNR model

The detected MTS signal amplitude scales as $A \cdot M(\beta, \phi_{\mathrm{fix}})$, where the overall factor A absorbs all β-independent contributions including optical power, molecular density, detector gain, and demodulation efficiency. The demodulation phase ϕ_{fix} is held constant at the experimentally optimized value throughout the measurement series. The noise at the modulation frequency ω_m was observed to increase linearly with β over the investigated range; this behavior is attributed to residual amplitude modulation from the EOM, which arises from parasitic etalon effects at

Optics EXPRESS

the crystal faces and produces a coherent intensity modulation at ω_m whose amplitude grows in proportion to the applied phase modulation depth. Modeling this contribution as $N(\beta) = 1 + \eta\,\beta$, where η is a dimensionless noise slope determined by the crystal face reflectivity and the balanced detector's common-mode rejection, and including a small β-independent floor S_0 from coherent electronic pickup at ω_m, the SNR takes the form of Eq. (11),

$$\mathrm{SNR}(\beta) = \frac{A \cdot M(\beta, \phi_{\mathrm{fix}})}{N(\beta)} + S_0\,.$$

At small β the signal grows linearly ($M \propto \beta$) while the noise remains near unity ($N \approx 1$), so the SNR rises; at large β the noise term dominates and the SNR decreases, producing an optimum at intermediate modulation depth.

Funding. German Federal Ministry of Research, Technology and Space (50WM2260A).

Disclosures. The authors declare no conflicts of interest.

Data availability. Data underlying the results presented in this paper are not publicly available at this time but may be obtained from the authors upon reasonable request.

References

1. T. Schuldt, M. Gohlke, M. Oswald, *et al.*, "Optical clock technologies for global navigation satellite systems," GPS Solut. **25**(3), 83 (2021).
2. V. Schkolnik, K. Döringshoff, F. B. Gutsch, *et al.*, "JOKARUS - design of a compact optical iodine frequency reference for a sounding rocket mission," EPJ Quantum Technol. **4**(1), 9 (2017).
3. K. Döringshoff, F. B. Gutsch, V. Schkolnik, *et al.*, "Iodine Frequency Reference on a Sounding Rocket," Phys. Rev. Appl. **11**(5), 054068 (2019).
4. F. Kuschewski, J. Wüst, M. Oswald, *et al.*, "COMPASSO mission and its iodine clock: outline of the clock design," GPS Solut. **28**(1), 10 (2024).
5. J. M. Wüst, M. Oswald, M. Gohlke, *et al.*, "Optical iodine clocks for future GNSS," in *9th International Colloquium on Scientific and Fundamental Aspects of GNSS*, (Wrocław, Poland, 2024).
6. J. Ye, L. Robertsson, S. Picard, *et al.*, "Absolute frequency atlas of molecular i_2 lines at 532 nm," IEEE Trans. Instrum. Meas. **48**(2), 544–549 (1999).
7. J. H. Shirley, "Modulation transfer processes in optical heterodyne saturation spectroscopy," Opt. Lett. **7**(11), 537–539 (1982).
8. T. Schuldt, K. Döringshoff, E. V. Kovalchuk, *et al.*, "Development of a compact optical absolute frequency reference for space with 10^{-15} instability," Appl. Opt. **56**(4), 1101–1106 (2017).
9. W.-Y. Cheng, L. Chen, T. H. Yoon, *et al.*, "Sub-doppler molecular-iodine transitions near the dissociation limit (523–498 nm)," Opt. Lett. **27**(8), 571–573 (2002).
10. L. Chen, "High-Precision Spectroscopy of Molecular Iodine: From Optical Frequency Standards to Global Descriptions of Hyperfine Interactions and Associated Electronic Structure," Ph.D. thesis, University of Colorado, Boulder, USA(2005).
11. C. Philippe, D. Holleville, R. Le Targat, *et al.*, "A compact frequency stabilized telecom laser diode for space applications," in *International Conference on Space Optics — ICSO 2016*, N. Karafolas, B. Cugny, and Z. Sodnik, eds. (SPIE, (Biarritz, France, 2017), p. 107.
12. A. Nishiyama, S. Okubo, T. Kobayashi, *et al.*, "Measurement of transition frequencies and hyperfine constants of molecular iodine at 520.2 nm," J. Opt. Soc. Am. B **41**(10), 2290–2296 (2024).
13. S. Bennetts, G. D. McDonald, K. S. Hardman, *et al.*, "External cavity diode lasers with 5 khz linewidth and 200 nm tuning range at 1.55µm and methods for linewidth measurement," Opt. Express **22**(9), 10642–10654 (2014).
14. D. J. Hopper and E. Jaatinen, "Optimizing modulation transfer spectroscopy signals for frequency locking in the presence of depleted saturating fields," Appl. Opt. **47**(14), 2574–2582 (2008).
15. S. Matsunaga, R. Kato, M. Yoshiki, *et al.*, "Analysis of the interaction-length dependence of frequency stability in an iodine-stabilized nd:yag laser," Appl. Opt. **63**(8), 2078–2085 (2024).
16. S. Gerstenkorn and P. Luc, *Atlas du spectre d'absorption de la molécule d'iode: 14800–20000 cm^{-1}* (Éditions du Centre National de la Recherche Scientifique (CNRS), Paris, 1978).
17. K. Döringshoff, "Optical frequency references based on hyperfine transitions in molecular iodine," Ph.D. thesis, Humboldt-Universität zu Berlin (2018).
18. J. M. Palmer and B. G. Grant, *Effective Noise Bandwidth of Analog RC Filters and the Selection of Filter Parameters to Optimize Signal-to-Noise Ratio* (SPIE Press, Bellingham, WA, 2009), vol. PM184 of *SPIE Press Monograph*, pp. 297–304.
19. D. York, N. M. Evensen, M. L. Martínez, *et al.*, "Unified equations for the slope, intercept, and standard errors of the best straight line," Am. J. Phys. **72**(3), 367–375 (2004).

Optics EXPRESS

20. L. Gillespie and L. Fraser, "The normal vapor pressure of crystalline iodine," J. Am. Chem. Soc. **58**(11), 2260–2263 (1936).
21. A. Arie and R. L. Byer, "Absolute frequency stabilization of diode-pumped nd:yag lasers," Laser Phys. **4**, 387–391 (1994).
22. M. L. Eickhoff and J. L. Hall, "Optical frequency standard at 532 nm," IEEE Trans. Instrum. Meas. **44**(2), 155–158 (1995).
23. H.-M. Fang, S. C. Wang, L.-C. Liu, *et al.*, "Measurement of hyperfine splitting of molecular iodine at 532 nm by double-passed acousto-optic modulator frequency shifter," Jpn. J. Appl. Phys. **45**(4R), 2776–2779 (2006).
24. H.-M. Fang, S. C. Wang, and J.-T. Shy, "Pressure and power broadening of the a_{10} component of r(56) 32–0 transition of molecular iodine at 532 nm," Opt. Commun. **257**(1), 76–83 (2006).
25. G. W. Oehlert, "A note on the delta method," Am. Stat. **46**(1), 27–29 (1992).
26. B. N. Taylor and C. E. Kuyatt, "Guidelines for evaluating and expressing the uncertainty of NIST measurement results," NIST Technical Note 1297, National Institute of Standards and Technology, Gaithersburg, MD (1994). 1994 edition.
27. D. J. Hopper, "Investigation of laser frequency stabilisation using modulation transfer spectroscopy," Phd thesis, Queensland University of Technology (2008).
28. J. F. Eble and F. Schmidt-Kaler, "Optimization of frequency modulation transfer spectroscopy on the calcium $4\,^1s_0$ to $4\,^1p_1$ transition," Appl. Phys. B **88**(4), 563–568 (2007).
29. T. Preuschoff, M. Schlosser, and G. Birkl, "Optimization strategies for modulation transfer spectroscopy applied to laser stabilization," Opt. Express **26**(18), 24010–24019 (2018).
30. K. Ikeda, S. Okubo, M. Wada, *et al.*, "Iodine-stabilized laser at telecom wavelength using dual-pitch periodically poled lithium niobate waveguide," Opt. Express **28**(2), 2166–2178 (2020).
31. J. Barbarat, J. Gillot, H. Alvarez-Martinez, *et al.*, "Compact and transportable iodine frequency-stabilized laser," in *International Conference on Space Optics — ICSO 2018*, vol. 11180 of *Proceedings of SPIE* (2019), p. 111800T.
32. J. Hrabina, O. Acef, F. du Burck, *et al.*, "Comparison of molecular iodine spectral properties at 514.7 and 532 nm wavelengths," Measurement Science Review **14**(4), 213–218 (2014).
33. W.-Y. Cheng, L. Chen, T. H. Yoon, *et al.*, "Sub-doppler molecular-iodine transitions near the dissociation limit (523–498 nm): errata," Opt. Lett. **27**(12), 1076 (2002).
34. E. J. Zang, J. P. Cao, Y. Li, *et al.*, "Realization of four-pass I_2 absorption cell in 532-nm optical frequency standard," IEEE Trans. Instrum. Meas. **56**(2), 673–676 (2007).
35. W. J. Riley, "Handbook of frequency stability analysis," NIST Special Publication 1065, National Institute of Standards and Technology, Washington, DC (2008).
36. W. J. Riley, "The bandwidth dependence of time domain frequency stability measurements," Hamilton Technical Services web site (2020). Stable32 frequency stability analysis documents.